Check for updates

Graphene-Assisted Synthesis of 2D Polyglycerols as Innovative Platforms for Multivalent Virus Interactions

Ehsan Mohammadifar, Vahid Ahmadi, Mohammad Fardin Gholami, Alexander Oehrl, Oleksandr Kolyvushko, Chuanxiong Nie, Ievgen S. Donskyi, Svenja Herziger, Jörg Radnik, Kai Ludwig, Christoph Böttcher, Jürgen P. Rabe, Klaus Osterrieder, Walid Azab, Rainer Haag,* and Mohsen Adeli*

2D nanomaterials have garnered widespread attention in biomedicine and bioengineering due to their unique physicochemical properties. However, poor functionality, low solubility, intrinsic toxicity, and nonspecific interactions at biointerfaces have hampered their application in vivo. Here, biocompatible polyglycerol units are crosslinked in two dimensions using a graphene-assisted strategy leading to highly functional and water-soluble polyglycerols nanosheets with 263 ± 53 nm and 2.7 ± 0.2 nm average lateral size and thickness, respectively. A single-layer hyperbranched polyglycerol containing azide functional groups is covalently conjugated to the surface of a functional graphene template through pH-sensitive linkers. Then, lateral crosslinking of polyglycerol units is carried out by loading tripropargylamine on the surface of graphene followed by lifting off this reagent for an on-face click reaction. Subsequently, the polyglycerol nanosheets are detached from the surface of graphene by slight acidification and centrifugation and is sulfated to mimic heparin sulfate proteoglycans. To highlight the impact of the two-dimensionality of the synthesized polyglycerol sulfate nanosheets at nanobiointerfaces, their efficiency with respect to herpes simplex virus type 1 and severe acute respiratory syndrome corona virus 2 inhibition is compared to their 3D nanogel analogs. Four times stronger in virus inhibition suggests that 2D polyglycerols are superior to their current 3D counterparts.

1. Introduction

Synthetic 2D nanomaterials (2DNs) have attracted wide attention in the past several years, due to the possibility of tuning their physicochemical and optoelectronic properties by manipulating their structure and functionality.[1] They are emerging as new vectors for different biomedical applications because of their unique mechanical and physicochemical characteristics including mechanical strength, flexibility, high surface area, high loading capacity, and photothermal, photodynamic, and antimicrobial properties.[2] However, major concerns regarding health risks, poor functionality, and solubility as well as nonspecific interactions at biointerfaces are serious challenges for their in vivo applications.[3] The strong structure-property relationships of 2DNs open up new avenues to overcome the aforementioned challenges via controlled synthetic methods.[4] In order to synthesize new 2DNs with

Dr. E. Mohammadifar, V. Ahmadi, Dr. A. Oehrl, Dr. C. Nie,
Dr. I. S. Donskyi, Prof. R. Haag
Institut für Chemie und Biochemie
Freie Universität Berlin
Takustrasse 3, 14195 Berlin, Germany
E-mail: haag@zedat.fu-berlin.de

M. F. Gholami, Prof. J. P. Rabe
Department of Physics and Integrative Research Institute
for the Sciences IRIS Adlershof
Humboldt-Universität zu Berlin
Newtonstrasse 15 and Zum Großen Windkanal 2, 12489 Berlin, Germany

O. Kolyvushko, Prof. K. Osterrieder, Dr. W. Azab
Institut für Virologie
Robert von Ostertag-Haus
Zentrum für Infektionsmedizin
Freie Universität Berlin
Robert-von-Ostertag-Str. 7-13, 14163 Berlin, Germany

Dr. I. S. Donskyi, Dr. J. Radnik
BAM – Federal Institute for Material Science and Testing Division
of Surface Analysis, and Interfacial Chemistry
Unter den Eichen 44-46, 12205 Berlin, Germany

Dr. S. Herziger, Dr. K. Ludwig, Dr. C. Böttcher
Forschungszentrum für Elektronenmikroskopie and Core Facility
BioSupraMol
Institut für Chemie und Biochemie Freie Universität Berlin
Fabeckstrasse 36a, 14195 Berlin, Germany

Prof. K. Osterrieder
Department of Infectious Diseases and Public Health
Jockey Club College of Veterinary Medicine and Life Sciences
City University of Hong Kong
Kowloon Tong, Hong Kong

Prof. M. Adeli
Department of Chemistry
Faculty of Science
Lorestan University
Khorramabad, Iran
E-mail: adeli.m@lu.ac.ir

The ORCID identification number(s) for the author(s) of this article can be found under https://doi.org/10.1002/adfm.202009003.

**ADVANCED
SCIENCE NEWS**
www.advancedsciencenews.com

**ADVANCED
FUNCTIONAL
MATERIALS**
www.afm-journal.de

diverse atomic structure, configurations, and alluring structure-dependent properties, the mechanism of their synthetic route and reaction parameters should be fully understood. Examples of well-defined 2DNs obtained by known mechanisms were reported for special applications.[5] The template-assisted synthetic strategies, including vat photopolymerization, electron beam lithography, nanocontact printing, dip-pen lithography, and photolithography, are well recognized as precise and reliable approaches to construct a wide range of 2DNs.[6] In spite of their efficiency, such approaches are expensive and in the most cases cannot be used for the high scale production of 2DNs. On-surface reactions using colloidal templates, however, are straightforward, scalable, and cost-effective approaches by which a variety of 2DNs can be synthesized.[7] The efficiency of this approach strongly depends on the interactions between monomers and the template.[8] In this method, monomers are stabilized on the template by noncovalent interactions,[9] and the mobility of monomers facilitates their self-rearrangement as well as formation of defects or cracks during polymerization.[10] However, the monomers could also come off the template, which lead to side reactions in solution and by-products that are difficult to remove from the main product.[11] With this approach the interactions between the template and monomers should be much stronger than between the solvent and monomers. This challenge limits the versatility of on-surface reactions using colloidal templates.

Covalent attachment of monomers on the surface of a template decreases the side reaction of template-desorbed monomers and results in more defined products with less impurity. This approach is, in particular, useful for functional (macro) monomers, which is difficult to deploy on the surface of a template. The critical point in the covalent approach is the attachment of monomers on the surface of the template by easily cleavable bonds, allowing for later detachment of the 2DNs from the template by external factors. Hyperbranched polyglycerol (hPG) is a polyfunctional, biocompatible, and water-soluble macromolecule with low non-specific interactions at biointerfaces. hPG is used for many biomedical applications ranging from drug delivery to pathogen interactions.[12] According to a previous in vivo toxicology study of intravenous injection of hPG with a molecular weight of 10 kDa demonstrated a serum half-life of the compound of 12 days.[13] Recently, it was shown that the attachment of this polymer on the surface of 2D templates resulted in functional 2D platforms with a high potential in biomedical applications.[12c,14] For example, their sulfated analogs were used as extracellular matrix mimics for the efficient virus binding and inhibition.[15]

They are 2D heparan-mimicking scaffolds with high surface area that attach to viral glycoproteins through electrostatic interactions and inhibit virus attachment, which is the first step of infection. Accordingly, heparan-mimicking compounds have been proposed as potential infection inhibitors against a number of pathogens, including SARS-CoV-2, which is currently causing a pandemic of historic proportions.[16] The electrostatic interaction of angiotensin-converting enzyme 2 and heparan sulfate with a positively charged patch on the receptor binding domain of the SARS-CoV-2 spike glycoprotein lends support to this hypothesis.[17] However, the toxicity of the graphene template on which polyglycerol branches are attached is a challenging issue which negates the advantages of these systems.[15a]

Therefore, production of template-free 2D polyglycerols is a big step toward water soluble and highly functional 2DNs with high biocompatibility and great potential for virus inhibition.

In this work, graphene sheets were used as flexible templates to construct 2D polyglycerols in solution. In this synthetic strategy, polyglycerol branches with 10% azide groups (hPG-N_3(10%)) were conjugated to the surface of graphene sheets by pH sensitive linkers and they were laterally crosslinked by a copper-catalyzed click reaction. Tripropargylamine was adsorbed on the surface of polyglycerol-functionalized graphene sheets and used as a crosslinker. The association of tripropargylamine with the graphene surface and lifting off this reagent by a controlled heating diminished the risk of intersheet crosslinking and resulted in 2D polyglycerol upon acidification and centrifugation. Virus-nanosheet interactions showed that sulfated polyglycerol nanosheets are more active than their 3D nanogel analogs, which highlights the critical role of topology in virus inhibition and steric shielding. Sulfated polyglycerol nanosheets as heparan sulfate mimics were also able to strongly inhibit SARS-CoV-2.

2. Results and Discussion

Graphene sheets with polyglycerol coverage have recently shown great potential as antimicrobial and antitumor systems.[15b,d,18] The toxicity of the graphene platform and related health risks are challenging issues for future developments. Accordingly, we have designed a synthetic strategy to produce graphene free 2D polyglycerol as a new class of 2D functional nanomaterials for future biomedical applications. In our current work, graphene was used as a platform for the synthesis of 2D polyglycerols due to the following the rationale: i) graphene surfaces are inert against usual reactions under mild conditions and, therefore, do not interfere with the reactions in our study; ii) the loading and lifting-up of the cross-linker through which lateral crosslinking is performed in a controlled manner is based on structure and π-conjugated system of graphene; iii) graphene can be functionalized by straightforward organic reactions; and iv) graphene is a colloidal template and dispersible in solvents. Therefore, we can take advantage of both solution and solid states of graphene. Thermally reduced graphene oxide with a lateral size in the range of 500 nm to 2 µm bearing dichlorotriazine functional groups (G-Trz) was synthesized[19] and post-functionalized by 3-(4-(dimethoxymethyl)phenoxy)propan-1-amine (DMPA) to obtain a platform (G-linker) with the ability of covalent attachment to the diol groups of polyglycerol through acid cleavable acetal bonds (**Figure 1**).[20] Then hPGol with 10% azide functionalization (hPG-N_3 (10%)) was conjugated to the pH sensitive linkers to create a polyglycerol coverage on the surface of graphene sheets (G-hPG). Crosslinking of polyglycerol coverage by Cu-catalyzed azide/alkyne click reaction and separation of the crosslinked coverage by acidification resulted in graphene-free 2D hPG (2D-hPG). The key point in this synthetic strategy was to adsorb the crosslinker on the surface of hPG-functionalized graphene sheets and exclude any free tripropargylamine to avoid inter-template crosslinking (Figure 1).
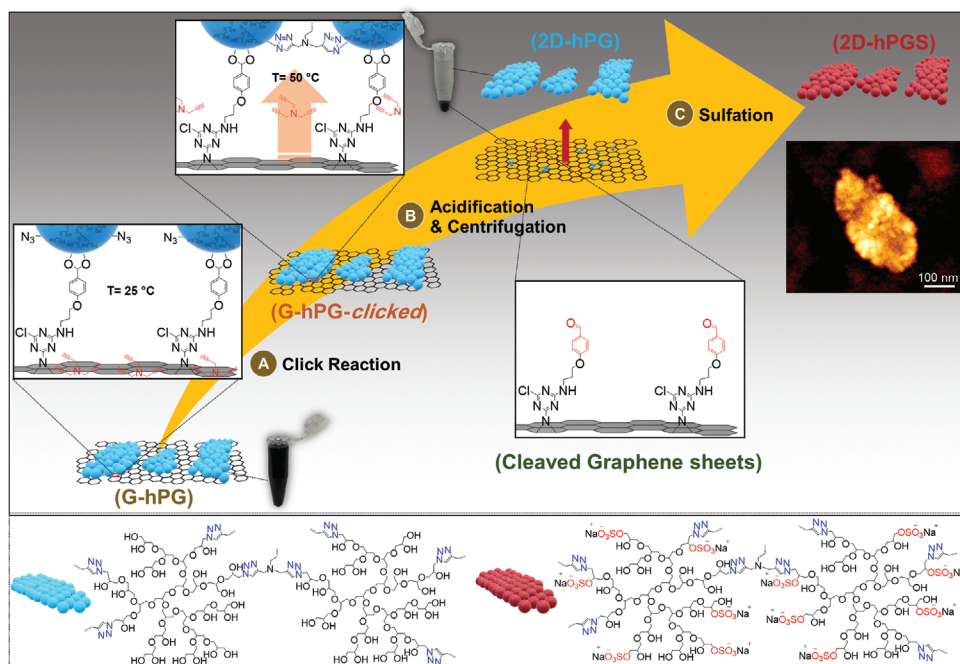
Figure 1. Schematic illustration and synthetic route for 2D hyperbranched polyglycerol. 2D-hPG can be formed on both sides of graphene but for simplification it is shown only on one side. Vial in the bottom-left shows the aqueous dispersion of graphene sheets with a polyglycerol coverage. Vial in the top-middle displays the aqueous solution after click reaction and acidification. While the graphene template is precipitated in the bottom of vial upon centrifugation, 2D polyglycerol remains in the supernatant. Finally, the 2D-hPG is sulfated and the inset shows an SFM image of the final multivalent 2D-hPGS nanosheets.

In order to synthesize a graphene template with pH-sensitive linkers, 2,4,6-trichloro-1,3,5-triazine was conjugated on the surface of thermally reduced graphene oxide (G) by a nitrene [2+1] cycloaddition reaction at ambient conditions.[19] The ratio of dichlorotriazine functional groups to the number of carbon atoms of graphene, the so-called density of functional groups, was 1/45 and 1/49 according to elemental and thermogravimetric analysis, respectively (Equation S1, Supporting Information). These results are consistent with our previous data, indicating the reproducibility of this functionalization method. The peak components ranging from 285 to 289 eV in the highly resolved C1s X-ray photoelectron spectroscopy (XPS) spectrum of G-Trz were assigned to the contribution of C—N and C—Cl bonds of dichlorotriazine groups (**Figure 2**b).[14b,15b,19b,21] In the IR spectrum of G-Trz, the absorbance bands at 1450–1550 cm^{-1} are assigned to C=C and C=N bonds of dichlorotriazine rings, which is another indication for the functionalization of graphene (Figure S4c, Supporting Information).[19b]

DMPA, as a pH-sensitive linker, was synthesized according to the reported method in literature with a slight modification (Scheme S1a, Supporting Information).[20b] A nucleophilic reaction between DMPA and G-Trz resulted in the G-linker template with the ability to covalently attach to the hPG through acid cleavable bonds (Scheme S1b, Supporting Information). Survey XPS spectra showed that the G-linker was composed of carbon, nitrogen, and oxygen elements (Figure 2a). An increased oxygen/carbon ratio in the XPS survey spectrum and decreased C—C/C=C component in the C1s spectrum of the G-linker were indications for the attachment of DMPA to the surface of G-Trz. Elemental analysis showed a decrease in the nitrogen content

upon attachment of DMPA to the surface of G-Trz. Since the carbon content of DMPA is higher than its nitrogen content, this result is a further indication of the post-modification of G-Trz by DMPA (Table S1, Supporting Information). The infrared (IR) spectrum of G-linker showed absorbance bands at 1100 and 2900 cm^{-1}, which are assigned to the C—O and aliphatic C—H bonds of DMPA moieties, respectively, conjugated to the surface of G-Trz (Figure S4d, Supporting Information).

Then hPG-N$_3$(10%) units were conjugated to the surface of G-linker by benzacetal moieties in the presence of catalytic amount of PTSA and G-hPG with a polyglycerol coverage was obtained (Scheme S1b, Supporting Information).[20a] The non-attached polyglycerols were removed by a 100 kDa ultrafiltration membrane to avoid undesired 3D crosslinking. An intense oxygen peak at 530.0 eV in the survey XPS spectra of G-hPG was due to the polyglycerol branches attached to the surface of the graphene template (Figure 2a). In the highly resolved C1s XPS spectrum, the peak components at 286.1 and 284.6 eV correspond to the C—O and C=C bonds of polyglycerol and graphene fragments (Figure 2d). Thermogravimetric analysis (TGA) and XPS showed 73% and 75% polyglycerol content for G-hPG, respectively (**Figures 2**d and **3**a). The IR spectrum of G-hPG showed absorbance bands at 1100, 2100, 2900, and 3400 cm^{-1}, which are assigned to the C—O, azide, aliphatic C—H, and hydroxyl groups, respectively (Figure 3b). In the proton nuclear magnetic resonance (^{1}H NMR) spectrum of G-hPG, signals at 3.2–4.2, 7.3, and 7.8 ppm were assigned to the protons of backbone of polyglycerol and aromatic protons of DMPA, respectively (Figure 3e).

The reversibly linked polyglycerol-azide on G-hPG was then crosslinked via Cu^I-catalyzed click reaction between

**ADVANCED
SCIENCE NEWS**

www.advancedsciencenews.com

**ADVANCED
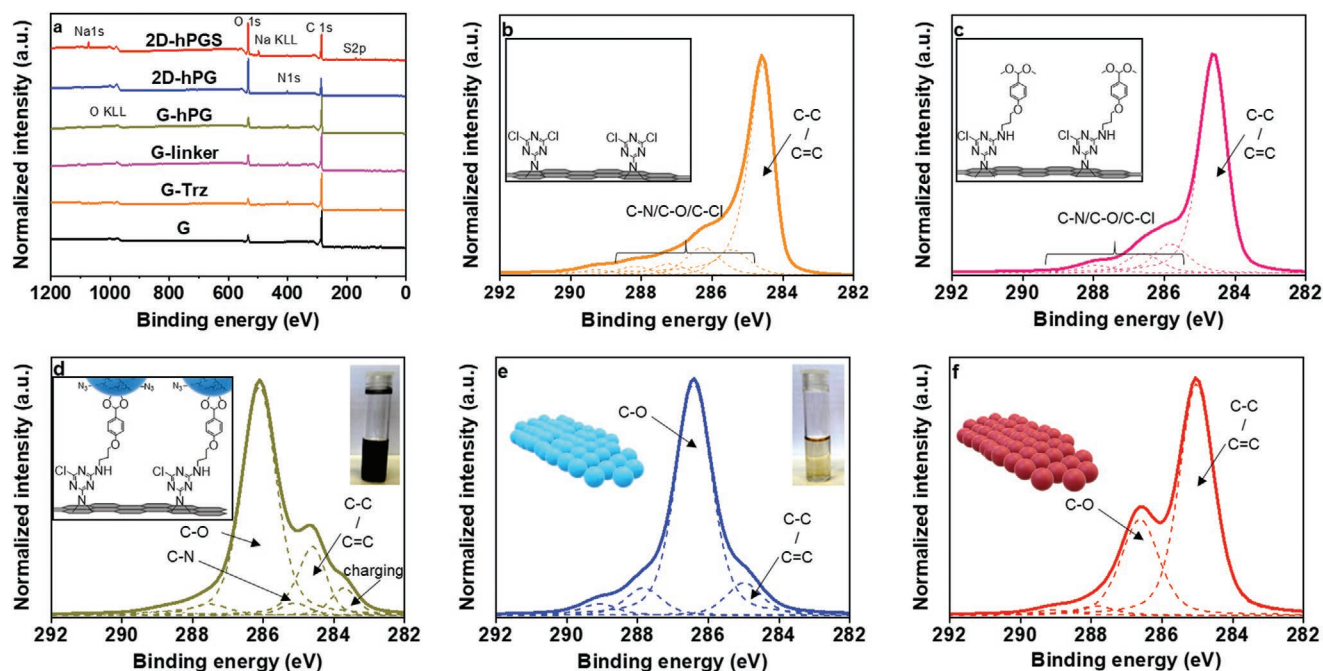FUNCTIONAL
MATERIALS**

www.afm-journal.de

Figure 2. a) Survey XPS spectra of the synthesized materials. Highly resolved XPS C1s spectra of b) G-Trz, c) G-linker, d) G-hPG, e) 2D-hPG, and f) 2D-hPGS. The main components are denoted on each spectrum. For further details of the assigned components see Table S4, Supporting Information. Inset: (d and e) are photographs of aqueous solutions of G-hPG and 2D-hPG, respectively.
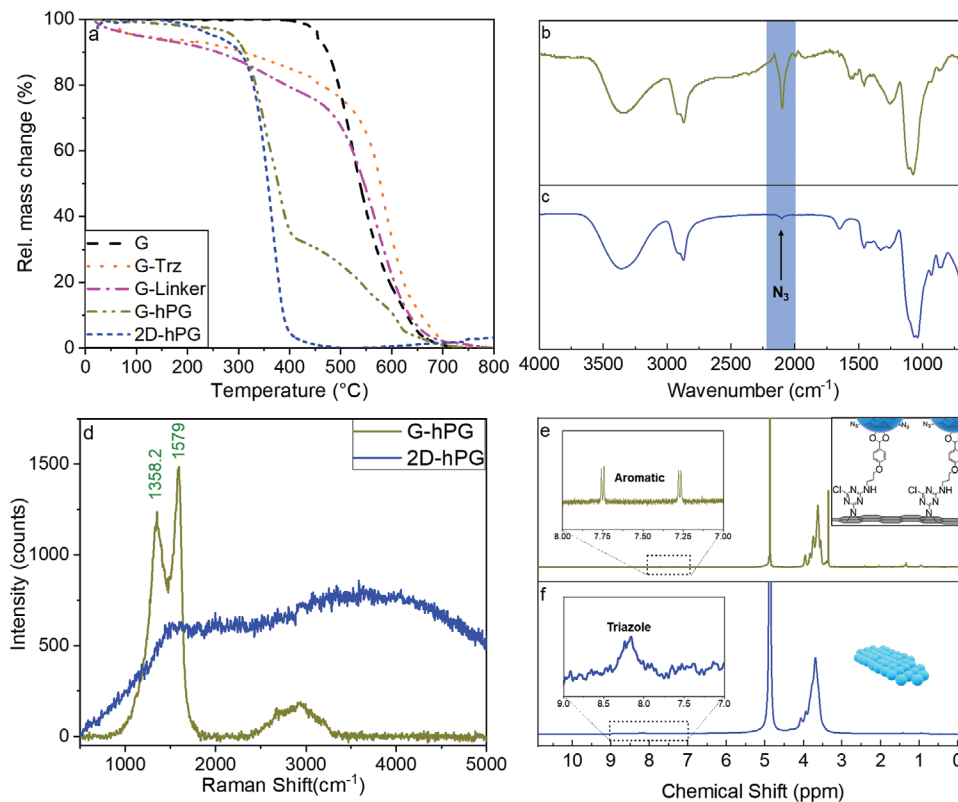

Figure 3. a) TGA thermograms of G, G-Trz, G-linker, G-hPG, and 2D-hPG. IR spectra of b) G-hPG and c) 2D-hPG. d) Raman spectra of G-hPG and 2D-hPG. ^{1}H-NMR spectra of e) G-hPG and f) 2D-hPG.

tripropargylamine and the azide groups selectively at the graphene interface. Tripropargylamine was loaded onto the surface of the graphene platform by π–π interactions. After loading, the product was purified to exclude free tripropargylamine that had not adsorbed onto the template. Confining tripropargylamine between the polyglycerol coverage and the graphene platform diminished the risk of inter-sheet crosslinking (Figure 1).

The click reaction was monitored by recording the IR spectra of the reaction mixture at intervals and checking the intensity of the azide band at 2100 cm^{-1} (Figure S5f, Supporting Information). The end point of reaction was realized by the disappearance of the azide band in the IR spectra. 2D polyglycerol (2D-hPG) sheets were subsequently detached from the graphene template by cleaving the acetal bonds in acidic solution (pH 4) and separated by subsequent centrifugation (Figure 1; Scheme S1, Supporting Information). Raman spectra of 2D-hPG did not show the D and G peaks of graphene, signifying the complete removal of template from the final product (Figure 3d). However, TGA showed ≈25% of hPG left on the surface of graphene after acid cleavage of 2D polyglycerol (Figure S7, Supporting Information).

The composition, size, and the morphology of 2D-hPG were investigated by different spectroscopic and microscopic methods as well as elemental and thermal analysis. A change in the component corresponding to C—C/C=C bonds in the highly resolved C1s XPS spectrum of 2D-hPG confirmed successful detachment of the graphene template from the polyglycerol nanosheets (Figure 2e; Tables S3 and S4, Supporting Information). Moreover, the triazole proton signal at 8 ppm in the ^{1}H NMR spectrum of 2D-hPG is an indication for the crosslinking of polyglycerol branches via click reaction (Figure 3f). Next the 2D-hPG was sulfated to obtain 2D-hPG sulfate (2D-hPGS) as an extracellular matrix mimic for the pathogen interactions. Elemental analysis showed 7.9 wt%

sulfur content for 2D-hPGS, which had been correlated to the sulfation of 58% of the hydroxyl groups of its precursor. A S2p peak component in the XPS survey spectrum (Figure 2a) and a change in the highly resolved C1s XPS spectrum of 2D-hPGS (Figure 2f) as well as absorbance bands of S=O bonds at 1200 cm^{-1} in the IR spectrum of this compound (Figure S5g, Supporting Information) indicated the successful sulfation of 2D-hPG.[15a,22] The negative surface charge of 2D-hPGS also corresponded to the sodium sulfate groups which are created upon sulfation (**Figure 5**h).

Scanning force microscopy in quantitative imaging mode (SFM-QI) and in tapping mode (TM-SFM) were used in order to investigate the lateral size, precise thickness, and morphology in addition to other properties of 2D-hPGS, such as stiffness and energy dissipation. We used freshly cleaved muscovite mica as a substrate of atomically flat and clean support for deposition of the 2D-hPGS. SFM-QI was used for precise height measurements and TM-SFM height images for lateral and morphological measurements at ambient conditions (22–25 °C and 30–35% rH). Those SFM methodologies demonstrated sheet-like structures distributed on the substrate (**Figure 4**a–c). These islands showed a typical average height of 2.7 ± 0.2 nm (Figure 5b,d) and 263 ± 53 nm average lateral dimension (error being standard deviation) (Figure 4; Figure S7g, Supporting Information). Since the hydrodynamic diameter of a single hPG macromolecule, measured by dynamic light scattering in water, is 5.34 ± 0.29 nm (Figure S8a, Supporting Information), we counted this thickness for a single layer 2D-hPG at ambient conditions. The observed average height for 2D-hPGS was assigned to the monolayer nanosheets at their partially compressed state due to lower water content at the mica surface compared to aqueous solution. To further quantify the two-dimensionality of the synthesized 2D-hPGS, their aspect ratio was calculated via dividing the maximum lateral length
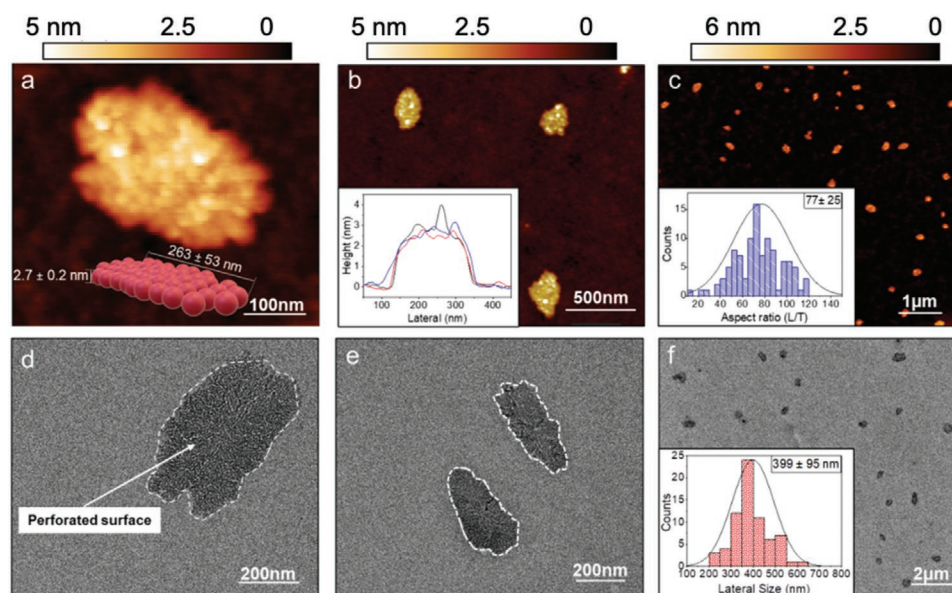

Figure 4. Characterization of polyglycerol nanosheets by different microscopic methods. a–c) SFM images of 2D-hPGS, deposited onto muscovite mica surface with different magnifications. Inset of Figure 4b,c is height profiles and aspect ratios of 2D-hPGS sheets, respectively. d–f) Transmission electron microscopy (TEM) images of 2D-hPGS. Inset of Figure 4f is lateral size of 2D-hPGS.
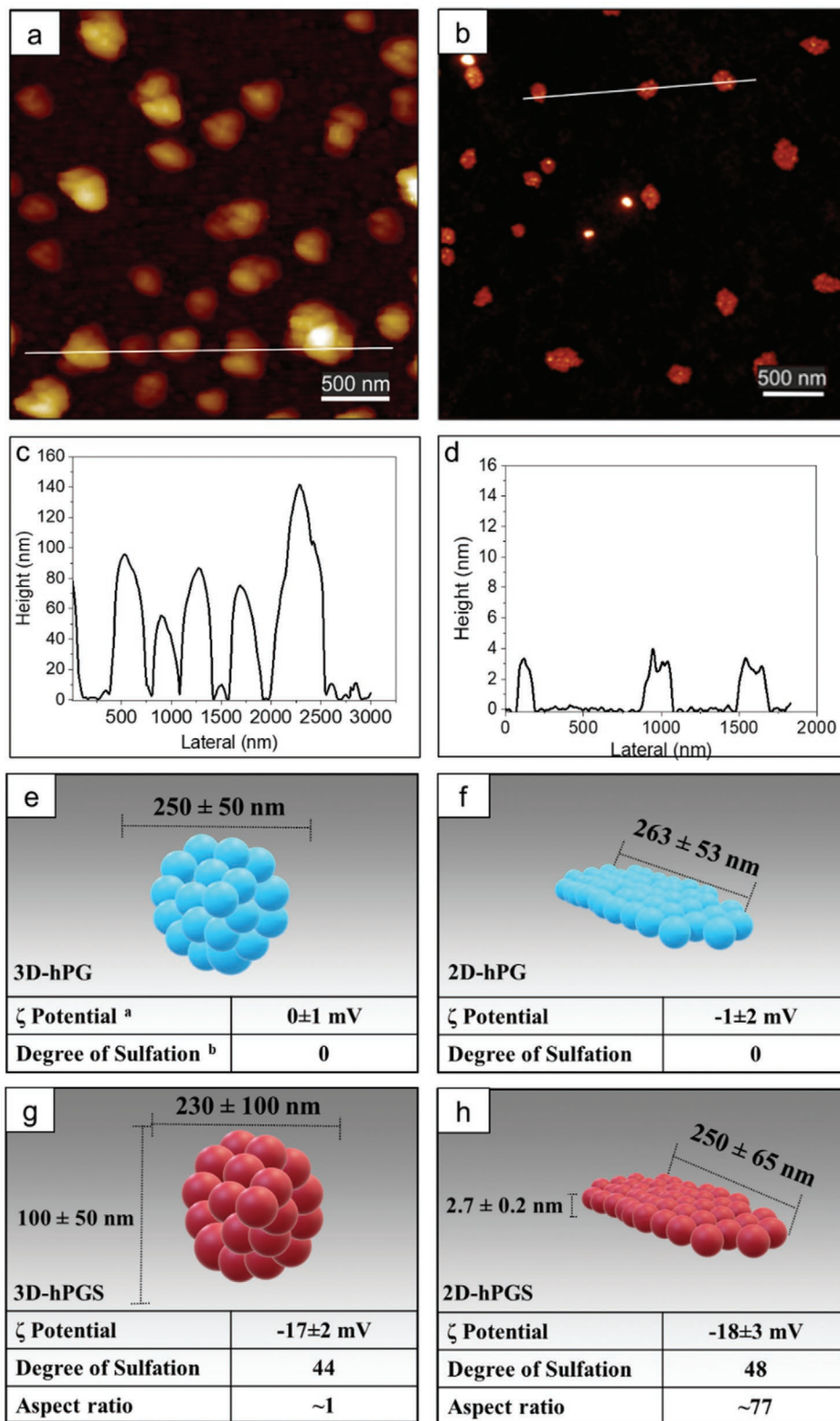
**ADVANCED
SCIENCE NEWS**
www.advancedsciencenews.com

**ADVANCED
FUNCTIONAL
MATERIALS**
www.afm-journal.de

Figure 5. SFM and height profile of a,c) 3D-hPGS and b,d) 2D-hPGS. e–h) Comparison of the properties of sulfated and non-sulfated 2D and 3D poly-glycerols in terms of lateral size, height, surface charge, and functional groups. In Figure 5e, [a]the surface charges were measured by Zetasizer.[b] The percentage of hydroxyl groups, which were converted to sulfate groups, were calculated by elemental analysis based on the sulfur content.

by thickness. Considering the spherical or ellipsoidal structure and an aspect ratio close to one for hPG, a mean aspect ratio of 77 was achieved for the 2D-hPGS. (Figure 4c inset). Transmission electron microscopy showed sheet-like structures with clear edges and perforated surface for 2D-hPGS (Figure 4d–f). Additionally, scanning electron microscopy showed a bumpy surface with 250 ± 65 nm average lateral size for 2D-hPG (Figure S6, Supporting Information).

The successful production of 2D-hPG sheets by click reaction was further investigated by setting up a control experiment, where the G-hPG (without the crosslinking agent) was stirred in acidic solution at room temperature for 24 h and then centrifuged. The supernatant was dialyzed by a 100 kDa membrane but no detectable compound was obtained. Because the cleaved polyglycerol branches were not crosslinked, they were small enough to leave the dialysis tube (Figure S3c, Supporting Information).

In order to highlight the role of graphene as the template in the synthesis of 2D-hPG, a control reaction was performed. In this reaction, hPG-N_3 (10%) units were crosslinked by tripropargylamine but in the absence of the graphene template (Figure S3d, Supporting Information). This control reaction resulted in small clusters of the hPG with random dimensions from 2 to 6 nm and aspect ratio close to unity, confirming the
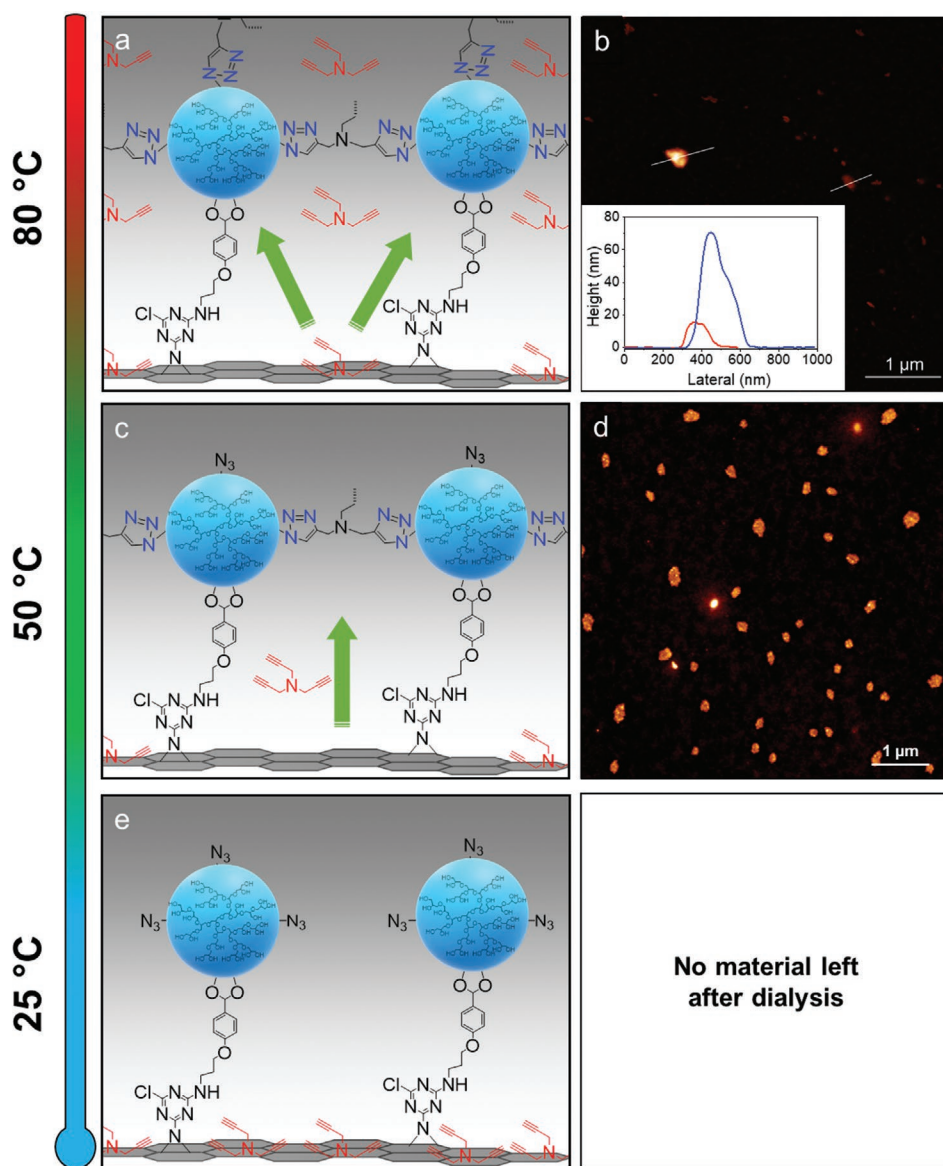

Figure 6. Representation of the key role of temperature in the synthesis of 2D-hPG. a) At 80 °C tripropargylamine molecules were able to leak from the polyglycerol coverage sublayers and inter-sheet crosslinking resulted in 3D structures. b) TM-SFM height images showed 3D objects with heights between 5 and 70 nm. c) The optimized temperature to produce 2D-hPG was 50 °C, where tripropargylamine molecules caused lateral crosslinking. d) SFM-QI height images showed successful crosslinking of polyglycerol macromolecules and production of 2D-hPG (height 2.7 nm). e) At 25 °C, the tripropargylamine molecules were not released from the graphene surface and crosslinking did not occurred. SFM experiments did not show any detectable object after acidification, centrifugation, and dialyzing the supernatant of the reaction.

critical role of graphene template for the production of 2D-hPG (Figure S3e, Supporting Information).

In order to prove the key role of temperature in releasing tripropargylamine molecules from the graphene surface, two additional control reactions were performed at room temperature and 80 °C. In these reactions, G-hPG with the loaded tripropargylamine molecules were stirred at the above-mentioned temperatures and they were monitored by spectroscopy and microscopy methods. While no significant decrease of the azide band in the IR spectrum of reaction mixture was observed at room temperature, it completely disappeared at 80 °C after 6 h (**Figure 6**a,b; Figure S5b, Supporting Information). However, SFM measurements showed a non-regular 3D morphology for the reaction product at 80 °C with a particle height between 5 and 70 nm (Figure 6b and inset). These control reactions confirmed the key role of the temperature in the production of 2D-hPG. At room temperature, tripropargylamine molecules were not released from graphene template significantly. Therefore an efficient click reaction and lateral crosslinking did not occur (Figure 6e; Figure S5a, Supporting

Information). However, at 80 °C tripropargylamine molecules were able to leak from the polyglycerol coverage into the reaction environment, leading to inter-sheet crosslinking and 3D objects (Figure 6b). These results are supported by our previous reports, in which increasing the temperature to 50–60 °C triggered the release of small molecules from the surface of graphene sheets.[14b]

In order to highlight the critical role of two dimensionality in bio-nano interactions, 3D analogs of 2D-hPG and 2D-hPGS (3D-hPG and 3D-hPGS, respectively) with similar average sizes were synthesized.[23] The detailed synthetic procedure and characterization are explained in the Supporting Information. SFM-QI mode was used to investigate 3D-hPGS at their hydrated state by immobilizing them within DI water at the mica interface (coated with poly-l-lysine layer). The cross section images of the 3D-hPGS nanogels revealed structures with 100 ± 50 nm and 230 ± 100 nm average height and lateral sizes, respectively (Figure 5a,c; Figure S8, Supporting Information). The difference between the morphology of 2D-hPG and 3D-hPG can be visually and quantitatively understood by
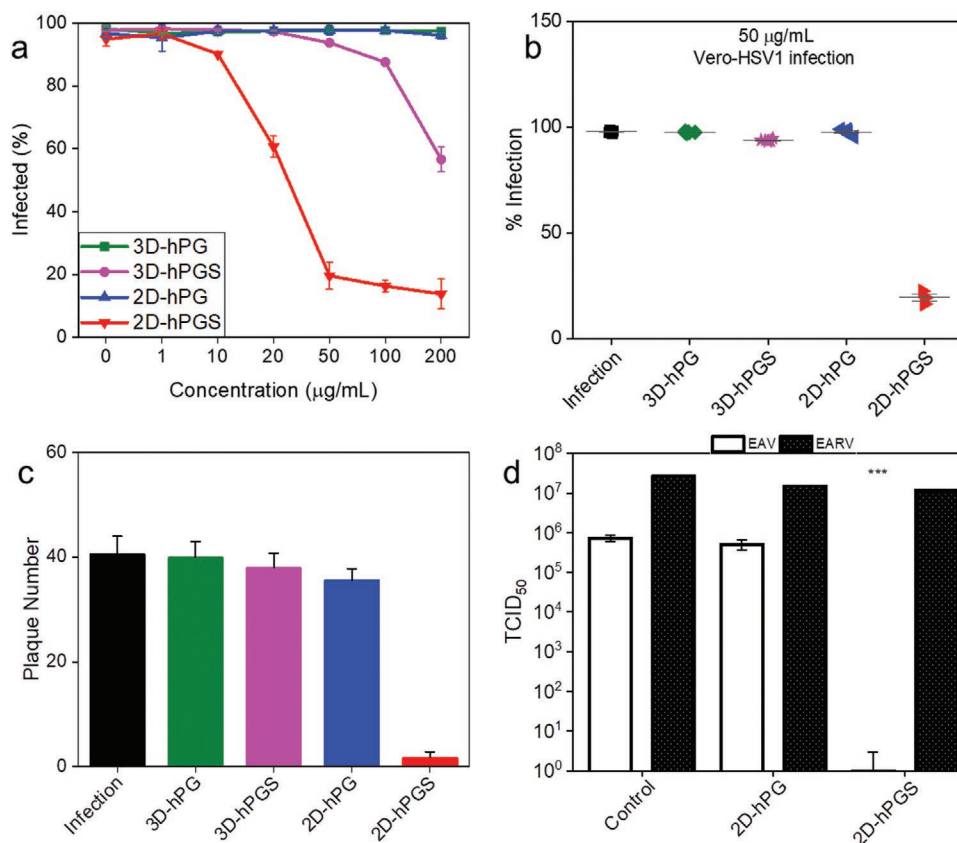

Figure 7. Comparative inhibition effects of 2D-hPG and their 3D analogs on viruses in susceptible cells. a) Concentration-dependent inhibition of HSV-1 infection on Vero E6 cells. Cells were infected with HSV-1 at MOI of 1 using different concentrations of the compounds as indicated. After 20 h of infection, the percentage of infected cells was analyzed by flow cytometry. b) Reduction of HSV-1 infection in Vero E6 cells at 50 μg mL^{-1}. HSV-1 (MOI = 1) was mixed with different compounds and added to cells. After 20 h of infection, the percentage of infected cells was analyzed by flow cytometry. c) Plaque reduction assay of HSV-1 with 3D-hPG, 3D-hPGS, 2D-hPG, and 3D-hPGS (concentration: 50 μg mL^{-1}) on Vero E6 cells. Vero E6 cells were grown in a 24-well plate and infected for 1 h with 50 PFU per well of HSV-1 in the presence or absence of 50 μg mL^{-1} of 2D and 3D compounds. At 48 h after infection, the number of plaques was quantified with inverted fluorescence microscope. d) Inhibitory effects of 2D compounds on enveloped and non-enveloped viruses. Reduction of tissue culture infection dose 50 (TCID$_{50}$) was used to measure the effects of 2D-hPGS on two viruses, equine rhinitis A virus (ERAV) and equine arteritis virus (EAV). Serial tenfold dilution of ERAV or EAV was added to RK-13 or BD cells, respectively, in the presence or absence of 2D-hPG and 2D-hPGS (50 μg mL^{-1}). Virus titer was determined after 4 days as described in the Supporting Information and Experimental Section.

considering their aspect ratio and overall topography. While 2D-hPG showed a sheet-like structure with average height of 2.7 ± 0.2, the average height of 3D-hPG was 100 ± 50 nm in the hydrated state.

2D-hPGS and 3D-hPGS as heparan sulfate mimics were expected to show low toxicity and efficient interactions with HS-binding domains on viral glycoproteins; particularly herpes virus gB and gC. Accordingly, the cytotoxicity of these nanomaterials and their ability for virus inhibition was investigated. While 2D-hPGS and 3D-hPGS did not show a significant cytotoxicity in vitro (Figure S9, Supporting Information), they efficiently inhibited infection of cells by enveloped viruses, including herpes simplex virus type 1 (HSV-1) on Vero E6 cells (**Figure 7**a–c) and equine arteritis virus (EAV) on bovine dermal (BD) cells (Figure 7d). Next, the efficiency of 2D-hPGS to inhibit HSV-1 infection on Vero E6 cells was determined. Different concentrations (ranging from 1 to 200 µg mL^{-1}) of 2D-hPGS were incubated with HSV-1 (at a multiplicity of infection (MOI) of 1) and applied to Vero E6 cells. After 24 h, infected cells were quantified using flow cytometry. A strong inhibition of infection at a concentration of 50 µg mL^{-1} with a half-maximal inhibitory concentration (IC$_{50}$) of 20 µg mL^{-1} (≈ 1.3 nm) (Figure 7a,b) against HSV-1 was observed for 2D-hPGS. In contrast, the 3D-hPGS did not cause a significant inhibition of infection at 50 µg mL^{-1} and its IC$_{50}$ was four times higher than the 2D analog (Figure 7a,b). Similar results of the inhibitory potential of the 2D-hPGS were determined by a plaque reduction assay. For a comparative

study all the candidates at a concentration of 50 µg mL^{-1} were mixed with HSV-1 (50 PFU (plaque-forming units)) and incubated with Vero E6 cells. To restrict virus spread from cell-to-cell, the cell monolayer was overlaid with 0.5% carboxymethylcellulose medium. Only 2D-hPGS showed a strong and significant reduction in plaque numbers (Figure 7c). From this data, it can be clearly understood that the ability of 2D-hPGS to inhibit the infection is much higher than 3D-hPGS, highlighting the critical role of morphology and two-dimensionality in shielding this nano-biointerface. Interestingly, the 2D-hPGS did not inhibit infection of RK-13 cells by equine rhinitis A virus (EARV) a non-enveloped small RNA virus (Figure 7d). Although EARV has a heparan sulfate-binding motif, it seems that this virus enters into the cells through a sialic acid-mediated pathway rather than HS-binding domains.[24] This may explain why the 2D-hPGS did not block EARV infection. Taken together, both 2D-hPGS and 3D-hPGS were able to specifically interact with HS-binding domains on viral proteins of enveloped viruses but 2D analogs showed stronger inhibitory effect than 3D-hPGS. This could be attributed to the 2D feature of 2D-hPGS, because, at a similar weight, they have a higher surface area than their 3D counterparts. In 2D-hPGS, more sulfate groups are accessible, which results in stronger interaction with the HS receptors on the surface of the virus. However, in 3D-hPGS, many of sulfate groups are hidden because they are present inside the gel and not accessible for interaction with virions. In addition to the large available surface area, energy
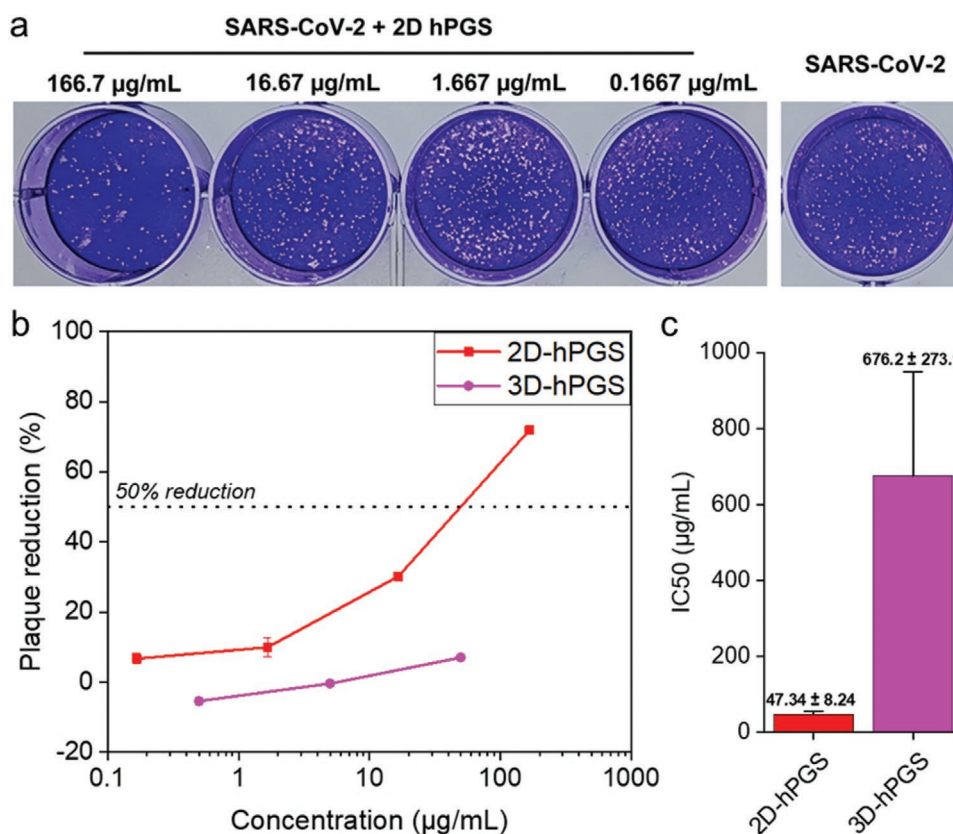

Figure 8. a) Representative images for the plaque reduction by 2D-hPGS. b) Plaque reduction ratios for the 2D-hPGS and 3D-hPGS at different concentrations. c) The obtained IC$_{50}$ values from plaque reduction for 2D-hPGS and 3D-hPGS.

requirement in creating multivalent interactions are often much smaller in the case of lower dimensionality.[15d,23,25]

The ability of the synthesized nanomaterials for coronavirus (SARS-CoV-2) inhibition was investigated by plaque reduction assay (**Figure 8**). Recently it was reported that heparin could inhibit the interaction of the spike glycoprotein (S) of SARS-CoV-2 with its cognate receptor.[17b,26] Consistent with the HSV-1 inhibition data, 2D-hPGS showed an IC50 value of 47.34 ± 8.24 µg mL^{-1} (≈3 nM, Equation S7, Supporting Information). This is likely due to binding of negatively charged 2D-hPGS to the positively charged patch at the receptor-binding domain of the S protein of SARS-CoV-2. This positively charged patch facilitated virus binding to cell surface heparan sulfate and explain the higher infectivity of SARS-CoV-2.[17b] Blocking the positively charged patch with a highly negative-charged inhibitor could decrease the binding of SARS-CoV-2 to the host cells surface and inhibit virus infection. The effective inhibition of SARS-CoV-2 by 3D-hPGS was much lower than 2D-hPGS, which again indicated the key role of two-dimensionality at this interface. 2D-hPGS showed no clear cellular toxicity at a concentration of 200 µg mL^{-1}, which supports its potential application as an inhibitor for SARS-CoV-2 (Figure S9, Supporting Information).

3. Conclusion

We have developed a unique bottom-up approach to synthesize 2D-hPG using a graphene-assisted strategy. Sulfation of 2D-hPG resulted in an extracellular matrix mimic with the ability of blocking the infection with representative enveloped viruses, including HSV-1 and SARS-CoV-2. Controlling the lateral crosslinking of polyglycerol branches by noncovalent interactions between the crosslinker and the graphene template was the key point of this synthetic approach. A salient aspect of this approach is that versatile polyfunctional 2DNs can be readily fabricated using different crosslinkers or through accurate post-modification of the obtained 2D hPG. In addition, we showed how two-dimensionality plays a crucial role for virus interactions by mimicking the cellular surface due to the high aspect ratio and multivalent interactions of 2D-hPGS.

Supporting Information

Supporting Information is available from the Wiley Online Library or from the author.

Conflict of Interest

The authors declare no conflict of interest.

Data Availability Statement

Research data are not shared.

[1] a) M. Xu, T. Liang, M. Shi, H. Chen, *Chem. Rev.* **2013**, *113*, 3766; b) K. Kang, S. Xie, L. Huang, Y. Han, P. Y. Huang, K. F. Mak, C.-J. Kim, D. Muller, J. Park, *Nature* **2015**, *520*, 656; c) H. Zhang, *ACS Nano* **2015**, *9*, 9451; d) G. Galeotti, F. De Marchi, E. Hamzehpoor, O. MacLean, M. Rajeswara Rao, Y. Chen, L. V. Besteiro, D. Dettmann, L. Ferrari, F. Frezza, P. M. Sheverdyaeva, R. Liu, A. K. Kundu, P. Moras, M. Ebrahimi, M. C. Gallagher, F. Rosei, D. F. Perepichka, G. Contini, *Nat. Mater.* **2020**, *19*, 874; e) K. Zhang, T. H. Lee, J. H. Cha, H. W. Jang, J.-W. Choi, M. Mahmoudi, M. Shokouhimehr, *Sci. Rep.* **2019**, *9*, 13739.

[2] a) G. Liu, H. Qin, T. Amano, T. Murakami, N. Komatsu, *ACS Appl. Mater. Interfaces* **2015**, *7*, 23402; b) P. Payamyar, B. T. King, H. C. Öttinger, A. D. Schlüter, *Chem. Commun.* **2016**, *52*, 18; c) D. Wang, W. Zhou, R. Zhang, J. Zeng, Y. Du, S. Qi, C. Cong, C. Ding, X. Huang, G. Wen, T. Yu, *Adv. Mater.* **2018**, *30*, 1803569; d) M. Li, Z. Luo, Y. Zhao, *Sci. China: Chem.* **2018**, *61*, 1214.

[3] a) L. M. Guiney, X. Wang, T. Xia, A. E. Nel, M. C. Hersam, *ACS Nano* **2018**, *12*, 6360; b) Z. Wang, W. Zhu, Y. Qiu, X. Yi, A. von dem Bussche, A. Kane, H. Gao, K. Koski, R. Hurt, *Chem. Soc. Rev.* **2016**, *45*, 1750; c) M. Fojtů, W. Z. Teo, M. Pumera, *Environ. Sci.: Nano* **2017**, *4*, 1617; d) H. Y. Mao, S. Laurent, W. Chen, O. Akhavan, M. Imani, A. A. Ashkarran, M. Mahmoudi, *Chem. Rev.* **2013**, *113*, 3407.

[4] a) K. H. Lee, H. S. Yu, S.-I. Kim, S. P. Moon, J.-Y. Hwang, S. W. Kim, *J. Alloys Compd.* **2019**, *790*, 93; b) L. Zhang, W. Liang, *J. Phys. Chem. Lett.* **2017**, *8*, 1517.

[5] a) X. Feng, A. D. Schlüter, *Angew. Chem., Int. Ed.* **2018**, *57*, 13748; b) I. Castano, A. M. Evans, H. Li, E. Vitaku, M. J. Strauss, J.-L. Brédas, N. C. Gianneschi, W. R. Dichtel, *ACS Cent. Sci.* **2019**, *5*, 1892; c) A. Faghani, M. F. Gholami, M. Trunk, J. Müller, P. Pachfule, S. Vogl, I. Donskyi, M. Li, P. Nickl, J. Shao, M. R. S. Huang, W. E. S. Unger, R. Arenal, C. T. Koch, B. Paulus, J. P. Rabe, A. Thomas, R. Haag, M. Adeli, *J. Am. Chem. Soc.* **2020**, *142*, 12976; d) S. Park, Z. Liao, B. Ibarlucea, H. Qi, H.-H. Lin, D. Becker, J. Melidonie, T. Zhang, H. Sahabudeen, L. Baraban, C.-K. Baek, Z. Zheng, E. Zschech, A. Fery, T. Heine, U. Kaiser, G. Cuniberti, R. Dong, X. Feng, *Angew. Chem., Int. Ed.* **2020**, *59*, 8218.

[6] a) P. van Assenbergh, E. Meinders, J. Geraedts, D. Dodou, *Small* **2018**, *14*, 1703401; b) Y. Ke, S. Ye, P. Hu, H. Jiang, S. Wang, B. Yang, J. Zhang, Y. Long, *Mater. Horiz.* **2019**, *6*, 1380; c) M. Drost, F. Tu, L. Berger, C. Preischl, W. Zhou, H. Gliemann, C. Wöll, H. Marbach, *ACS Nano* **2018**, *12*, 3825.

[7] a) D. Cui, M. Ebrahimi, J. M. Macleod, F. Rosei, *Nano Lett.* **2018**, *18*, 7570; b) C. Tan, H. Zhang, *Nat. Commun.* **2015**, *6*, 7873; c) R. Dong, T. Zhang, X. Feng, *Chem. Rev.* **2018**, *118*, 6189.

[8] M. Lackinger, *Polym. Int.* **2015**, *64*, 1073.

[9] a) S. Kang, J. Lee, S. Ryu, Y. Kwon, K.-H. Kim, D. H. Jeong, S. R. Paik, B.-S. Kim, *Chem. Mater.* **2017**, *29*, 3461; b) J. D. Cojal González, M. Iyoda, J. P. Rabe, *Nat. Commun.* **2017**, *8*, 14717; c) D. Cui, M. Ebrahimi, F. Rosei, J. M. Macleod, *J. Am. Chem. Soc.* **2017**, *139*, 16732; d) D. P. Goronzy, M. Ebrahimi, F. Rosei, Arramel, Y. F. , S. De Feyter, S. L. Tait, C. Wang, P. H. Beton, A. T. S. Wee, P. S. Weiss, D. F. Perepichka, *ACS Nano* **2018**, *12*, 7445; e) A. D. Stroock, R. S. Kane, M. Weck, S. J. Metallo, G. M. Whitesides, *Langmuir* **2003**, *19*, 2466.

[10] O. Ourdjini, R. Pawlak, M. Abel, S. Clair, L. Chen, N. Bergeon, M. Sassi, V. Oison, J.-M. Debierre, R. Coratger, L. Porte, *Phys. Rev. B* **2011**, *84*, 125421.

[11] a) G. Wei, Y. Zhang, S. Steckbeck, Z. Su, Z. Li, *J. Mater. Chem.* **2012**, *22*, 17190; b) J. Wang, Z. Ouyang, Z. Ren, J. Li, P. Zhang, G. Wei, Z. Su, *Carbon* **2015**, *89*, 20.

[12] a) S. Abbina, S. Vappala, P. Kumar, E. M. J. Siren, C. C. La, U. Abbasi, D. E. Brooks, J. N. Kizhakkedathu, *J. Mater. Chem. B* **2017**, *5*, 9249; b) M. Calderón, M. A. Quadir, S. K. Sharma, R. Haag, *Adv. Mater.* **2010**, *22*, 190; c) H. Frey, R. Haag, *Rev. Mol. Biotechnol.* **2002**, *90*, 257.

[13] C. Holzhausen, D. Gröger, L. Mundhenk, C. K. Donat, J. Schnorr, R. Haag, A. D. Gruber, *J. Nanopart. Res.* **2015**, *17*, 116.

[14] a) Z. Tu, G. Guday, M. Adeli, R. Haag, *Adv. Mater.* **2018**, *30*, 1706709; b) Z. Tu, H. Qiao, Y. Yan, G. Guday, W. Chen, M. Adeli, R. Haag, *Angew. Chem., Int. Ed.* **2018**, *57*, 11198; c) Z. Tu, K. Achazi, A. Schulz, R. Mülhaupt, S. Thierbach, E. Rühl, M. Adeli, R. Haag, *Adv. Funct. Mater.* **2017**, *27*, 1701837.

[15] a) I. S. Donskyi, W. Azab, J. L. Cuellar-Camacho, G. Guday, A. Lippitz, W. E. S. Unger, K. Osterrieder, M. Adeli, R. Haag, *Nanoscale* **2019**, *11*, 15804; b) M. F. Gholami, D. Lauster, K. Ludwig, J. Storm, B. Ziem, N. Severin, C. Böttcher, J. P. Rabe, A. Herrmann, M. Adeli, R. Haag, *Adv. Funct. Mater.* **2017**, *27*, 1606477; c) B. Ziem, J. Rahn, I. Donskyi, K. Silberreis, L. Cuellar, J. Dernedde, G. Keil, T. C. Mettenleiter, R. Haag, *Macromol. Biosci.* **2017**, *17*, 1600499; d) B. Ziem, W. Azab, M. F. Gholami, J. P. Rabe, N. Osterrieder, R. Haag, *Nanoscale* **2017**, *9*, 3774; e) B. Ziem, H. Thien, K. Achazi, C. Yue, D. Stern, K. Silberreis, M. F. Gholami, F. Beckert, D. Gröger, R. Mülhaupt, J. P. Rabe, A. Nitsche, R. Haag, *Adv. Healthcare Mater.* **2016**, *5*, 2922.

[16] a) V. Palmieri, M. Papi, *Nano Today* **2020**, *33*, 100883; b) C. Weiss, M. Carriere, L. Fusco, I. Capua, J. A. Regla-Nava, M. Pasquali, J. A. Scott, F. Vitale, M. A. Unal, C. Mattevi, D. Bedognetti, A. Merkoçi, E. Tasciotti, A. Yilmazer, Y. Gogotsi, F. Stellacci,

L. G. Delogu, *ACS Nano* **2020**, *14*, 6383; c) S. Talebian, G. G. Wallace, A. Schroeder, F. Stellacci, J. Conde, *Nat. Nanotechnol.* **2020**, *15*, 618.

[17] a) J. Lan, J. Ge, J. Yu, S. Shan, H. Zhou, S. Fan, Q. Zhang, X. Shi, Q. Wang, L. Zhang, X. Wang, *Nature* **2020**, *581*, 215; b) T. M. Clausen, D. R. Sandoval, C. B. Spliid, J. Pihl, C. D. Painter, B. E. Thacker, C. A. Glass, A. Narayanan, S. A. Majowicz, Y. Zhang, J. L. Torres, G. J. Golden, R. Porell, A. F. Garretson, L. Laubach, J. Feldman, X. Yin, Y. Pu, B. Hauser, T. M. Caradonna, B. P. Kellman, C. Martino, P. L. S. M. Gordts, S. L. Leibel, S. K. Chanda, A. G. Schmidt, K. Godula, J. Jose, K. D. Corbett, A. B. Ward, A. F. Carlin, J. D. Esko, *Biorxiv : the Preprint Server for Biology* **2020**, *183*, 1043.

[18] Z. Tu, V. Wycisk, C. Cheng, W. Chen, M. Adeli, R. Haag, *Nanoscale* **2017**, *9*, 18931.

[19] a) A. Setaro, M. Adeli, M. Glaeske, D. Przyrembel, T. Bisswanger, G. Gordeev, F. Maschietto, A. Faghani, B. Paulus, M. Weinelt, R. Arenal, R. Haag, S. Reich, *Nat. Commun.* **2017**, *8*, 14281; b) A. Faghani, I. S. Donskyi, M. Fardin Gholami, B. Ziem, A. Lippitz, W. E. S. Unger, C. Böttcher, J. P. Rabe, R. Haag, M. Adeli, *Angew. Chem., Int. Ed.* **2017**, *56*, 2675.

[20] a) M. Dimde, D. Steinhilber, F. Neumann, Y. Li, F. Paulus, N. Ma, R. Haag, *Macromol. Biosci.* **2017**, *17*, 1600190; b) D. Steinhilber, T. Rossow, S. Wedepohl, F. Paulus, S. Seiffert, R. Haag, *Angew. Chem., Int. Ed.* **2013**, *52*, 13538.

[21] G. Guday, I. S. Donskyi, M. F. Gholami, G. Algara-Siller, F. Witte, A. Lippitz, W. E. S. Unger, B. Paulus, J. P. Rabe, M. Adeli, R. Haag, *Small* **2019**, *15*, 1805430.

[22] a) C. S. Campelo, P. Chevallier, J. M. Vaz, R. S. Vieira, D. Mantovani, *Mater. Sci. Eng. C* **2017**, *72*, 682; b) I. Donskyi, M. Drüke, K. Silberreis, D. Lauster, K. Ludwig, C. Kühne, W. Unger, C. Böttcher, A. Herrmann, J. Dernedde, M. Adeli, R. Haag, *Small* **2018**, *14*, 1800189; c) M. Ferraro, K. Silberreis, E. Mohammadifar, F. Neumann, J. Dernedde, R. Haag, *Biomacromolecules* **2018**, *19*, 4524.

[23] P. Dey, T. Bergmann, J. L. Cuellar-Camacho, S. Ehrmann, M. S. Chowdhury, M. Zhang, I. Dahmani, R. Haag, W. Azab, *ACS Nano* **2018**, *12*, 6429.

[24] a) S. Warner, C. A. Hartley, R. A. Stevenson, N. Ficorilli, A. Varrasso, M. J. Studdert, B. S. Crabb, *J. Virol.* **2001**, *75*, 9274; b) E. E. Fry, T. J. Tuthill, K. Harlos, T. S. Walter, D. J. Rowlands, D. I. Stuart, *J. Gen. Virol.* **2010**, *91*, 1971.

[25] B. J. Reynwar, G. Illya, V. A. Harmandaris, M. M. Müller, K. Kremer, M. Deserno, *Nature* **2007**, *447*, 461.

[26] S. Y. Kim, W. Jin, A. Sood, D. W. Montgomery, O. C. Grant, M. M. Fuster, L. Fu, J. S. Dordick, R. J. Woods, F. Zhang, R. J. Linhardt, *Antiviral Res.* **2020**, *181*, 104873.